Energy xxx (xxxx) xxx

Contents lists available at ScienceDirect

Energy

journal homepage: www.elsevier.com/locate/energy

Novel designs of hybrid thermal energy storage system and operation strategies for concentrated solar power plant

Zhao Ma [a], Ming-Jia Li [a, *], K. Max Zhang [b], Fan Yuan [a]

[a] Key Laboratory of Thermo-Fluid Science and Engineering of MOE, School of Energy and Power Engineering, Xi'an Jiaotong University, Xi'an, Shaanxi, 710049, China
[b] Sibley School of Mechanical and Aerospace Engineering, Cornell University, Ithaca, NY, 14853, USA

ARTICLE INFO

Article history:
Received 23 April 2020
Received in revised form
16 October 2020
Accepted 9 November 2020
Available online xxx

Keywords:
Packed-bed thermal energy storage
Hybrid thermal energy storage system
Concentrated solar power plant
Realistic solar radiation
Annual performance

ABSTRACT

Packed-bed thermal energy storage (PBTES) has advantage of being relatively low cost, but suffers from low utility factor, compared with two-tank thermal energy storage (TTES). This paper proposes two new designs of hybrid thermal energy storage system (HTESS), consisting of PBTES and TTES, and corresponding operation strategies: HTESS-TS for thermocline storage and HTESS-OTC for outlet temperature control. Firstly, structures and operation strategies of HTESS-TS and HTESS-OTC are described in detail. Then, thermal and economic performances of HTESS and single-tank thermal energy storage system (STESS) only containing PBTES in stand-alone state are compared. Next, effects of cut-off temperature and thermal capacity of TTES are analyzed. Finally, under realistic solar radiation, annual performance of concentrated solar power plant (CSP) with different thermal energy storage systems are compared. Results show that compared with STESS, utility factors of HTESS-TS and HTESS-OTC are improved by 12.5% and 22.1% respectively. Meanwhile, unit cost of HTESS-OTC is 8.6% lower than that of STESS. In addition, for a broad range of outlet temperature limits, HTESS-OTC can maintain more stable outlet temperature, higher utility factor than STESS. Compared with STESS, annual generated electricity induced by HTESS-TS and HTESS-OTC increase by 9.8% and 14.1% respectively.

1. Introduction

Efficient utilization of solar energy has become an important mitigation strategy for global climate change [1]. However, due to the intermittent nature of solar resources, there is a mismatch between energy supply and demand. Concentrating solar power (CSP) [2] with thermal energy storage (TES) can play a critical role in our transition to a sustainable energy system as it can achieve large-scale energy storage capacity at a relatively low costs and generate electricity continuously throughout a day [3].

There are three kinds of thermal energy storage: sensible thermal energy storage [4], latent thermal energy storage [5,6] and thermochemical energy storage [7]. At present, two-tank thermal energy storage (TTES) with hot tank and cold tank has widely been employed in CSP commercial plant [8,9]. For example, Crescent Dunes tower plant (110MWe) and Gema solar tower plant (19.9 MWe) are equipped with molten salt TTES [8]. In terms of economics, TTES is capital intensive because of the large amount of expensive molten salt stored in the molten salt tank as heat transfer fluid (HTF) and heat storage media [10]. To further reduce the cost of TES, packed bed thermal energy storage (PBTES) using one storage tank and replacing most of molten salt with cheap solid fillers to store heat has been widely studied, which showed that the capital costs of PBTES can be reduced by 20–37% compared to TTES [11].

However, due to the finite heat transfer rate between solar fillers and HTF, there exists a temperature gradient along the axial direction of PBTES, known as thermocline [4], causing the phenomenon that the outlet temperature of PBTES starts to rise at the end time of charging process and to decline at the end time of discharging process [12]. Meanwhile, to ensure the safe operation of the solar collector and power block, the outlet temperature of a thermal energy storage system (TESS) should be lower than the charging cut-off temperature $T_{ch,cut\text{-}off}$ in charging process and higher than the discharging cut-off temperature $T_{dis,cut\text{-}off}$ in discharging process [13]. Constrained by the outlet temperature limits, the total heat storage capacity of PBTES cannot be fully utilized [4]. In addition, in the successive charging-discharging process, the

* Corresponding author.
E-mail address: mjli1990@xjtu.edu.cn (M.-J. Li).

https://doi.org/10.1016/j.energy.2020.119281
0360-5442/

Nomenclature and units

A	area, m^2
C_{TES}	unit cost for thermal energy storage system, $\$\cdot kWh^{-1}$
C_{total}	total cost, \$
c	specific heat, $J\cdot kg^{-1}\cdot K^{-1}$
D	diameter, m
ESD	energy storage density, $J\cdot kg^{-1}$
H	height of storage tank, m
h	none-dimension height of storage tank
h_v	volumetric heat transfer coefficient, $W\cdot m^{-2}\cdot K^{-1}$
L	latent heat, $J\cdot kg^{-1}\cdot K^{-1}$
$\dot{m}$	mass flow rate of heat transfer fluid, $kg\cdot s^{-1}$
P	power, W
SM	solar multiply
T	temperature, K
t	time, s
u	velocity, $m\cdot s^{-1}$
W	generated electricity, MWh_e
x_{TTES}	nominal capacity ratio of TTES over HTESS

Greek symbols

η_{ex}	exergetic efficiency
$\eta_{PB,rated}$	*rated thermal-electricity efficiency of power block*
η_u	utility factor of capacity
λ	thermal conductivity, $W\cdot m\cdot K^{-1}$
ρ	density, $kg\cdot m^{-1}$
ϕ	void fraction

Subscripts

c	cold
ch	charging
dis	discharging
eff	effective
h	hot
nom	nominal
out	outlet
PB	power block
p	pressure
R	outer radius of solid particle
r	radial coordinate inside each solid particle
sto	storage
v	volumetric

Abbreviations

CSP	concentrated solar power
EPCM	encapsulated phase change material
HTESS	hybrid thermal energy storage system
HTF	heat transfer fluid
PBTES	packed-bed thermal energy storage
PCM	phase change material
STESS	single-tank thermal energy storage
TES	thermal energy storage
TTES	two-tank thermal energy storage

thickness of thermocline in PBTES can be extended and the utility factor further decreases [14].

Researchers around the world have worked on improving the utility factor of PBTES in three main areas: filler material [4], structure of PBTES [15], operation system and strategy [16].

For the filler materials, the high specific heat and thermal conductivity have beneficial effects on the utility factor of PBTES [15]. Li et al. [4] proposed a multi-layer PBTES with different solid filler materials, and found that the available heat storage capacity was improved by 10.5%, compared to single-layer PBTES. As the high density heat storage material, phase change material (PCM) can be encapsulated, known as encapsulated phase change material (EPCM), to replace solid fillers and packed in PBTES to improve the energy storage density [17]. Zhao and Cheng [18,19] optimized the EPCM ratio in PBTES packed with solid fillers and EPCM together, and their simulation results showed that compared with TTES, the available heat capacity of the PBTES with optimum EPCM ratio is greatly improved and the unit cost for heat storage decreases by 36.8%–39.2%. Li et al. [17,20] designed and experimentally tested a two-layer PBTES with EPCM of different diameters, and their experimental results showed that compared with single-diameter encapsulated PCM, the two-layer PBTES shows 12.3% improvement of heat storage rate and 13% increasing of heat storage density. However, as indicated in Ref. [21], in PBTES with EPCM, melting point of EPCM should be within the outlet temperature limits to achieve high utility factor [22], which is difficult for the choice of appropriate EPCM and impedes the application of PBTES with EPCM.

For the structure of PBTES, smaller filler size and larger height-over-diameter ratio for the storage tank lead to the improvement of utility factor [23], at the cost of larger (and more expensive) pump power [24]. Besides, the height of tank cannot exceed a certain value due to the limit of allowable strength [25].

For the operation system and operation, the utility factor of PBTES can be enhanced based on their original material and size through adjusting operation system and controlling system appropriately. Ju and Xu et al. [10] proposed a hybrid heat storage system consisting of a large PBTES and a small TTES. In this hybrid heat storage, the TTES is employed to store and release molten salt during solar radiation fluctuation, and it was found that the CSP plant with hybrid heat storage can continuously generate steady power during short-term fluctuation of solar radiation. However, the economic performance of the hybrid heat storage system was not discussed. Thermocline control methods [26,27], such as extraction method [28], injection method [29,30] and mixing method [26], were proposed by various researchers to improve the utility factor of PBTES. Geissbühler and Haselbacher et al. [27] compared the performance of extraction method, injection method and mixing method of thermocline controlling, and found that the mixing method shows the largest improvement of the utility factor by 38.8% compared with no thermocline controlling method.

The literature review above indicates that the majority of the existing studies are focused on the material and structure aspects of PBTES to improve the utility factor and that few papers exist concerning the operation and system, which has been suggested to boost the utility factor of PBTES largely. One existing work of hybrid heat storage system from Ju and Xu et al. [10] is proved to have the potential to improve the utility factor of PBTES. Meanwhile, there is a lack of economic analysis in studies of the operation system and strategy. On the other hand, for PBTES filled with EPCM, the thermal performance is dramatically affected by the relationship between melting temperature of EPCM and the outlet temperature limits. It might be difficult to obtain practical EPCM of suitable melting temperature satisfying the outlet temperature limits, which may hinder the realistic application of PBTES with EPCM. Thus, to make it easier for the choice of EPCM, it is needed to reduce effect of

outlet temperature limits on thermal performance of PBTES filled with EPCM and make sure PBTES can achieve relatively high utility factor no matter whether the melting point is within the outlet temperature limit or not. Therefore, this paper has two main goals: (1) to improve the utility factor of PBTES with EPCM, and (2) to reduce the effect of outlet temperature limits for easy application of PBTES with EPCM. To achieve these goals, based on the hybrid structure of heat storage system [10], hybrid thermal energy storage system (HTESS) and corresponding operation strategies are proposed with respect to the thermal energy storage system operation strategies.

This paper is organized as follows. Firstly, the hybrid thermal energy storage system and corresponding operation strategies are described in detail. Then, for the basic and standard evaluation, stand-alone thermal and economic performance of hybrid thermal energy storage systems and single-tank thermal energy storage system are compared. Next, to further explore the characteristics of HTESS, the effects of cut-off temperature during charging/discharging process and thermal capacity ratio of two-tank TES in HTESS are discussed. Finally, in order to test the realistic performance of thermal energy storage in CSP plant, an integration model of CSP plant is established and annual performance of CSP plant with different thermal energy storage systems under realistic solar radiation are discussed.

2. Description of hybrid thermal energy storage system and operation strategies

2.1. Hybrid thermal energy storage system and operation strategies

Due the existence of thermocline along the storage tank, PBTES cannot be in fully charged/discharged state [15]. To fully utilize the unused heat capacity of PBTES, two different designs of hybrid thermal energy storage system (HTESS) including a packed-bed thermal energy storage filled with EPCM and a two-tank thermal energy storage are proposed. As comparison, the single-tank thermal energy storage system (STESS) refers to the thermal energy storage that only contains the packed-bed thermal energy storage.

Fig. 1 shows the schematic diagram of single-tank thermal energy storage system and two new designs of hybrid thermal energy storage system. In HTESS, PBTES operates as the major thermal energy storage to store and release thermal energy, while the two-tank TES functions as the assistant thermal energy storage to fully utilize the discarded heat capacity in charging-discharging process with the purpose of guaranteeing the outlet temperature of thermal energy storage system within the allowable temperature range. According to different operation strategies of two-tank TES in HTESS, these two proposed designs of HTESS are HTESS with operation strategy TS (for Thermocline Storage as illustrated in Fig. 1 (b)) and HTESS with operation strategy OTC (for Outlet Temperature Control as illustrated in Fig. 1 (c)) respectively.

In HTESS with operation strategy TS (HTESS-TS), the two-tank thermal energy storage is employed to store the high-temperature and low-temperature thermal energy of thermocline lay in the PBTES during charging and discharging process respectively, which cannot be immediately utilized due to the limit of the cut-off outlet temperature. Then, the stored high-temperature and low-temperature heat transfer fluid in hot and cold tank is used for the next cycle of discharging process and charging process respectively and the utility factor of PBTES can be improved. Thus, this strategy of thermocline storage is the strategy TS. In HTESS operation strategy OTC (HTESS-OTC), the two-tank thermal energy storage is used to control the outlet temperature of HTESS satisfying the limits of outlet temperature and improve the utility factor of PBTES by extending the charging/discharging time. Thus, this strategy of outlet temperature controlling is the strategy OTC.

The operation strategies of HTESS-TS and HTESS-OTC can both be divided into 4 modes. Fig. 2 shows the schematic diagram of HTESS-TS and HTESS-OTC in different modes. As shown in this figure, the operation strategies of HTESS-TS and HTESS-OTC both can be is divided into 4 different modes: Mode TS-1, Mode TS-2, Mode OTC-1 and Mode OTC-2 for charging process, meanwhile Mode TS-3, Mode TS-4, Mode OTC-3 and Mode OTC-4 for discharging process. Table 1 illustrates characteristics of different modes for strategy TS and OTC.

Mode TS-1 and Mode OTC-1: it's in charging process and the outlet temperature of PBTES is lower than $T_{ch,cut\text{-}off}$. In these modes, hot heat transfer fluid flows from solar collector through the PBTES from the top port, releases heat to PBTES, then flows out of HTESS and is mixed with the HTF from power block to be heated in the solar collection block again. Meanwhile, the state of two-tank thermal energy storage doesn't change.

Mode TS-2 and Mode OTC-2: it's in charging process and the outlet temperature of PBTES is higher than $T_{ch,cut\text{-}off}$. For Mode TS-2, HTF flows through the PBTES first, then flows into hot tank of TTES to be stored, meanwhile the cold HTF flows out of cold tank and is mixed with the HTF from power block which then is heated in the solar collection. While for Mode OTC-2, hot HTF from solar collector

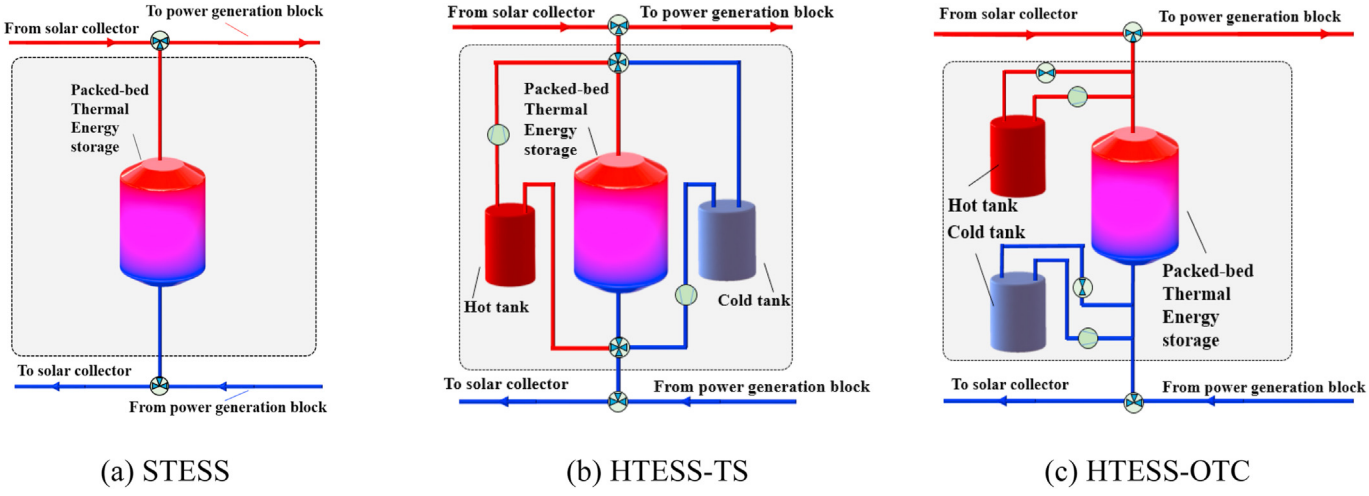

Fig. 1. Structural illustration of single-tank thermal energy storage system and two different hybrid thermal energy storage systems.

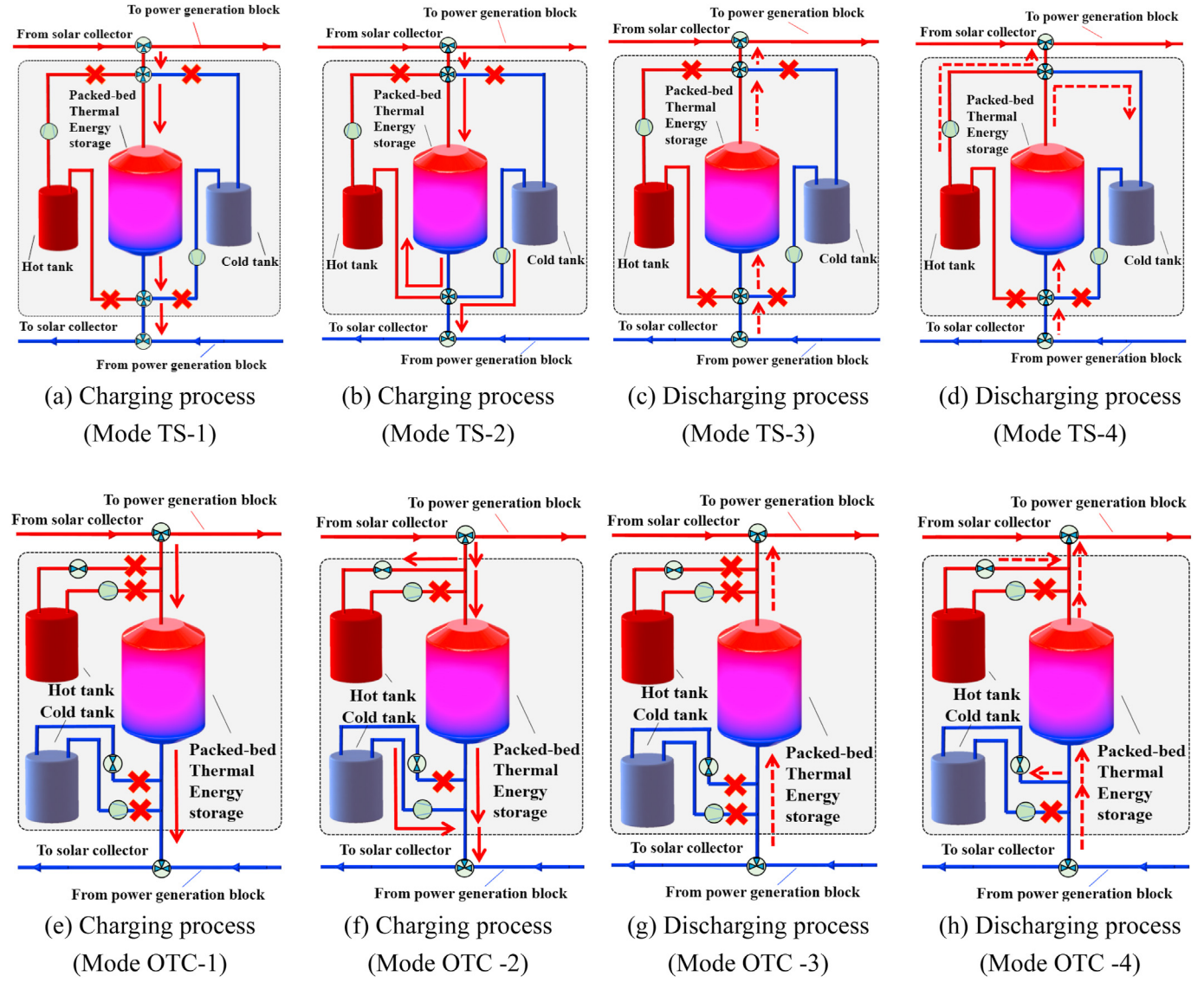

Fig. 2. Schematic diagrams of hybrid thermal energy storage system with operation strategy TS and OTC.

Table 1
Characteristics of different modes for strategy TS and OTC.

Process	Mode	Outlet temperature		State of two-tank TES
		Packed-bed TES	HTESS	
Charging	Mode TS-1	$< T_{ch,cut\text{-}off}$	$< T_{ch,cut\text{-}off}$	Not Running
	Mode OTC-1	$< T_{ch,cut\text{-}off}$	$< T_{ch,cut\text{-}off}$	Not Running
	Mode TS-2	$> T_{ch,cut\text{-}off}$	$< T_{ch,cut\text{-}off}$	Running
	Mode OTC-2	$> T_{ch,cut\text{-}off}$	$= T_{ch,cut\text{-}off}$	Running
Discharging	Mode TS-3	$> T_{dih,cut\text{-}off}$	$> T_{dih,cut\text{-}off}$	Not Running
	Mode OTC-3	$> T_{dih,cut\text{-}off}$	$> T_{dih,cut\text{-}off}$	Not Running
	Mode TS-4	$< T_{dih,cut\text{-}off}$	$> T_{dih,cut\text{-}off}$	Running
	Mode OTC-4	$< T_{dih,cut\text{-}off}$	$= T_{dih,cut\text{-}off}$	Running

Each mode of different operation strategies is explained as follows.

is distributed into PBTES and hot tank separately and the outflow of HTESS is the mixture of the fluid from PBTES and cold tank. And the mass flow rates of HTF in PBTES and TTES are determined to keep the outlet temperature of HTESS at $T_{ch,cut\text{-}off}$.

Mode TS-3 and Mode OTC-3: it's in discharging process and outlet temperature of PBTES is higher than $T_{dis,cut\text{-}off}$. Cold heat transfer fluid flows from power block through the PBTES from the bottom port, absorbs heat from PBTES, then flows out HTESS into power block. Meanwhile, the state of two-tank thermal energy storage doesn't change.

Mode TS-4 and Mode OTC-4: it's in discharging process and outlet temperature of PBTES is lower than $T_{dis,cut\text{-}off}$. For Mode TS-4,

HTF flows through the PBTES first and then flows into cold tank of TTES, meanwhile the hot HTF flows out of hot tank and then flows into power block. For Mode OTC-4, cold HTF flowing form power block into HTESS is distributed into PBTES and cold tank separately. The outflow of HTESS is the mixture of the fluid from PBTES and hot tank. And mass flow rates of HTF in PBTES and TTES are determined to keep the outlet temperature of HTESS at $T_{dis,cut\text{-}off}$.

The expected outlet temperature illustrations of HTESS-TS and HTESS-OTC in different modes are shown in Fig. 3 (a) and (b) respectively. As shown in Fig. 3 (a), in Mode TS-2 and Mode TS-4, the outflow of HTESS is from the cold and hot tank to guarantee the outlet temperature within the limit of outlet temperature respectively. As shown in Fig. 3 (b), in Mode OTC-2 and Mode OTC-4, the outflow of HTESS is the flow mixture of PBTES and TTES to guarantee the outlet temperature equals to $T_{ch,cut\text{-}off}$ and $T_{dis,cut\text{-}off}$ for charging and discharging process respectively.

2.2. Structural and operation parameters of thermal energy storage system

The sizes of STESS and HTESS (HTESS-TS and HTESS-OTC) need to be decided before comparing the thermal and economic performance of thermal energy storage. In present study, the thermal energy storage system is designed to meet the heat storage requirement of a certain CSP plant [31] with rated net power $P_{net,rated}$ of 100 MW_e, parasitic power consumption of 10.3%, rated thermal-electricity efficiency $\eta_{PB,rated}$ of 0.4116, and the heat storage time t_{store} is 8 h. The upper and lower half of PBTES are separately packed with high-melting-temperature PCM (HTPCM) and low-melting-temperature PCM (LTPCM) to improve the energy storage density [18].

The nominal heat storage capacity of thermal energy storage system is calculated by:

$$Q_{nom,total} = \frac{P_{net,rated} t_{store}}{(1 - x_{parasitic})\eta_{PB,rated}} \tag{1}$$

The nominal heat storage capacities of two-tank TES and packed-bed TES, which are denoted by $Q_{nom,TTES}$ and $Q_{nom,PBTES}$ respectively, can be obtained by Eq. (2) and Eq. (3).

$$Q_{nom,TTES} = x_{TTES} Q_{nom,total} \tag{2}$$

$$Q_{nom,PBTES} = (1 - x_{TTES}) Q_{nom,total} \tag{3}$$

where x_{TTES} represents the nominal capacity ratio of TTES over HTESS (HTESS-TS and HTESS-OTC), and is set to be 0.25 in this study.

Due to the limited structural strength, the height of the storage tank cannot exceed 16 m [32]. Similar with the heat storage tank of Andasol [15], heights of TTES and PBTES are both set to be 14 m. The diameters of TTES and PBTES can be calculated by Eq. (4).

$$D_{tank} = \sqrt{\frac{4Q_{nom}}{\pi ESD_v H}} \tag{4}$$

where Q_{nom} is the nominal capacity of thermal energy storage; H represents the tank height; ESD_v denotes the volumetric heat capacity density of thermal energy storage, where $ESD_{v,TTES}$ and $ESD_{v,PBTES}$ represent the volumetric heat capacity density of TTES and PBTES respectively and can be expressed as Eq. (5) and Eq. (6).

$$ESD_{v,TTES} = \rho_{HTF} c_{p,HTF} (T_h - T_c) \tag{5}$$

$$\begin{aligned} ESD_{v,PBTES} &= \varepsilon \rho_{HTF} c_{p,HTF} (T_h - T_c) \\ &+ 0.5(1-\phi)\left[(\rho c_p)_{HTPCM}(T_h - T_c) + (\rho L)_{HTPCM}\right] \\ &+ 0.5(1-\phi)\left[(\rho c_p)_{LTPCM}(T_h - T_c) + (\rho L)_{LTPCM}\right] \end{aligned} \tag{6}$$

where ρ and c_p are the density and specific heat separately, and subscript "HTF", "HTPCM" and "LTPCM" denote the heat transfer fluid, high-melting-temperature phase change material and low-melting-temperature phase change separately, ϕ is the porosity of PBTES, L denotes the latent heat of phase change material.

In this study, the inlet temperature of STESS and HTESS (HTESS-TS and HTESS-OTC) during charging and discharging process are set to be 600 °C and 300 °C respectively [31]. Binary nitrate molten salt, solar salt (60 wt % $NaNO_3$-40 wt % KNO_3), is adopted as HTF, meanwhile $NaNO_3$ and ternary carbonate (20 wt % Li_2CO_3- 60 wt % Na_2CO_3- 20 wt % K_2CO_3) are packed into PBTES as LTPCM and HTPCM respectively. Table 2 shows the thermo-physical properties of HTF, LTPCM and HTPCM [18].

The rated mass flow rate of fluid through thermal energy storage system during charging and discharging process can be calculated by Eq. (7)

Table 2
Thermo-physical properties of HTF, LTPCM and HTPCM [18].

Property	HTF-Solar salt	LTPCM	HTPCM
ρ/kg·m^{-3}	1857	2260	2380
c_p/J·kg^{-1}·K^{-1}	1500	1588	1590
λ/W·m^{-1}·K^{-1}	0.54	0.5	0.5
T_m/K	–	308	550
L/kJ·kg^{-1}	–	172	283

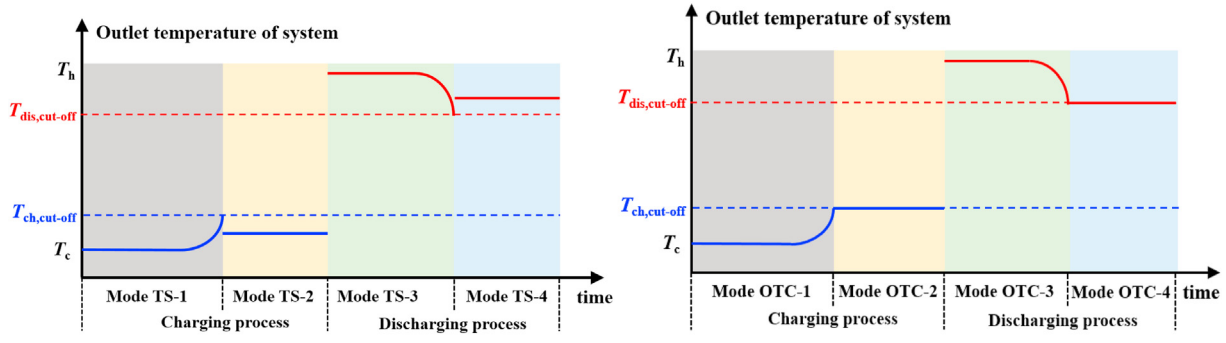

(a) HTESS-TS (b) HTESS-OTC

Fig. 3. Outlet temperature illustration of HTESS-TS and HTESS-OTC in different modes.

$$\dot{m}_{\mathrm{sto,rated}} = \frac{P_{\mathrm{net,rated}}}{(1 - x_{\mathrm{parasitic}})\eta_{\mathrm{PB,rated}} c_{p,\mathrm{HTF}}(T_{\mathrm{h}} - T_{\mathrm{c}})} \tag{7}$$

In simulations, the cut-off temperature difference $\Delta T_{\mathrm{cut-off}}$ for charging and discharging process is set to be the 30% of (T_{h}-T_{c}) [4,33], which means that the cut-off temperature is $T_{\mathrm{c}}+0.3(T_{\mathrm{h}}-T_{\mathrm{c}})$ for charging process and $T_{\mathrm{h}}-0.3(T_{\mathrm{h}}-T_{\mathrm{c}})$ for discharging process. Table 3 presents the calculated structural and operation parameters of STESS and HTESS (HTESS-TS/HTESS-OTC).

2.3. Mathematical model of PBTES

Fig. 4 depicts the schematic diagram of packed bed thermal energy storage. Two-phase D-C (Dispersion-Concentric) transient model is adopted to predict the heat transfer performance in PBTES. In the model establishment, some assumptions are employed:

(1) The radial heat transfer process is ignored, and the fluid flow and heat transfer can be regarded as one-dimensional process [34].
(2) The thermal energy storage is well insulated, and the heat loss is negligible.
(3) The thermo-physical properties of HTF and PCM are constant.

The governing equation for the HTF can be expressed as:

$$\frac{\partial(\phi\rho_{\mathrm{HTF}}c_{p,\mathrm{HTF}}T_{\mathrm{HTF}})}{\partial t} + \frac{\partial(\rho_{\mathrm{HTF}}c_{p,\mathrm{HTF}}uT_{\mathrm{HTF}})}{\partial x} = \frac{\partial}{\partial x}\left(\lambda_{\mathrm{HTF,eff}}\frac{\partial T_{\mathrm{HTF}}}{\partial x}\right) + h_{\mathrm{v}}(T_{\mathrm{PCM},R} - T_{\mathrm{HTF}}) \tag{8}$$

where T_{HTF} is the local temperature of HTF, ρ_{HTF} and $c_{p,\mathrm{HTF}}$ are the density and specific heat of HTF respectively, ϕ denotes the porosity of the PBTES, u represents the superficial velocity of HTF, $\lambda_{\mathrm{HTF,eff}}$ is the effective thermal conductivity of the HTF in the porous media, which can be calculated by Eq. (9) [35], $T_{\mathrm{s},R}$ is the surface temperature of EPCM, and h_{v} represents the volumetric heat transfer coefficient between HTF and EPCM.

$$\lambda_{\mathrm{HTF,eff}} = \lambda_{\mathrm{l}}\left[\frac{1 + 2\beta\varphi + (2\beta^3 - 0.1\beta)\varphi^2 + 0.05\varphi^3\exp(4.5\beta)}{1 - \beta\varphi}\right] \tag{9}$$

where the constants φ and β can be separately expressed as:

$$\varphi = 1 - \phi \tag{10}$$

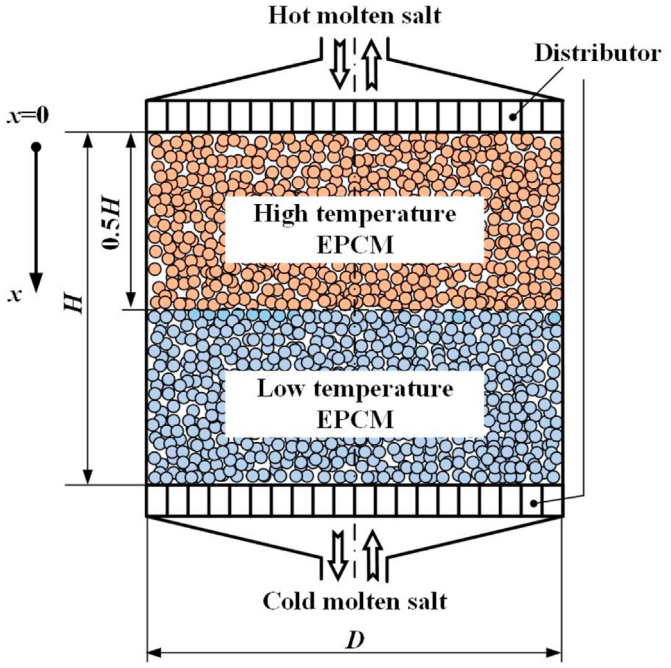

Fig. 4. Schematic diagram of packed bed thermal energy storage.

$$\beta = \frac{\lambda_{\mathrm{PCM}} - \lambda_{\mathrm{HTF}}}{\lambda_{\mathrm{PCM}} + 2\lambda_{\mathrm{HTF}}} \tag{11}$$

where λ_{HTF} and λ_{PCM} denote the thermal conductivity of HTF and PCM, respectively.

The superficial velocity u can be calculated by Eq. (12).

$$u = \frac{\dot{m}_{\mathrm{HTF}}}{\rho_{\mathrm{HTF}}A_{\mathrm{cross}}} \tag{12}$$

where A_{cross} represent the cross-section area of PBTES perpendicular to the axial direction.

h_{v} can be obtained by Refs. [34] :

$$h_{\mathrm{v}} = \frac{6(1-\phi)\lambda_{\mathrm{HTF}}\left[2 + 1.1Re_{\mathrm{p}}^{0.6}Pr^{1/3}\right]}{d_{\mathrm{p}}^2} \tag{13}$$

where Pr is the Prandtl number of HTF, d_{p} is the diameter of EPCM, and Re_{p} is the Reynolds number based on the diameter of EPCM.

In the EPCM part, the inner energy conversation equation is solved, and the heat transfer between the EPCM and HTF at the surface of EPCM can be adopted as the boundary condition. The

Table 3
Structural and operation parameters of STESS and HTESS (HTESS-TS/HTESS-OTC).

Parameter		STESS	HTESS(HTESS-TS/HTESS-OTC)	
		PBTES	TTES	PBTES
Structure	H_{tank}/m	14	14	14
	D_{tank}/m	23.4	15.1	20.3
	ϕ	0.34	0.34	0.34
	Q_{nom}/MWh$_{\mathrm{th}}$	2167.2	541.8	1625.4
Operation	T_{h}/°C	600	600	600
	T_{c}/°C	300	300	300
	$T_{\mathrm{ch,cut-off}}$/°C	390	390	390
	$T_{\mathrm{dis,cut-off}}$/°C	510	510	510
	$\dot{m}_{\mathrm{sto}}$/kg·s^{-1}	645.0	645.0	645.0

energy governing equation for EPCM can be expressed as:

$$\frac{\partial(\rho_{\mathrm{PCM}} c_{p,\mathrm{PCM}} T_{\mathrm{PCM}})}{\partial t} = \lambda_{\mathrm{PCM}} \left(\frac{\partial^2 T_{\mathrm{PCM}}}{\partial r^2} + \frac{2}{r} \frac{\partial T_{\mathrm{PCM}}}{\partial r} \right) \tag{14}$$

where T_{PCM} is the local temperature of EPCM, r denotes the radial coordinates of EPCM, ρ_{PCM} and $c_{p,\mathrm{PCM}}$ are respectively are the density and specific heat of EPCM. In this study, "effective heat capacity" method is employed to calculate the specific heat of PCM during phase transition [36], which can be expressed as Eq. (15).

$$c_{p,\mathrm{PCM,eff}} = \begin{cases} c_{p,\mathrm{PCM}}, & T < T_{\mathrm{m}} - \dfrac{\Delta T}{2} \\ c_{p,\mathrm{PCM}} + \dfrac{L_{\mathrm{PCM}}}{\Delta T}, & T_{\mathrm{m}} - \dfrac{\Delta T}{2} \le T < T_{\mathrm{m}} + \dfrac{\Delta T}{2} \\ c_{p,\mathrm{PCM}}, & T \ge T_{\mathrm{m}} + \dfrac{\Delta T}{2} \end{cases} \tag{15}$$

where ΔT is set to 2 K.

In STESS, the mass flow rate of HTF flowing through PBTES $\dot{m}_{\mathrm{PBTES}}$ is equal to $\dot{m}_{\mathrm{sto,rated}}$. In HTESS, the mass flow rate of HTF for PBTES and TTES is determined as presented in Fig. 5. As shown in Fig. 5 (a), when HTESS operates in strategy TS, the mass flow rate of HTF flowing through PBTES is constantly equal to $\dot{m}_{\mathrm{HTF,rated}}$, and in charging process mass flow rate of HTF flowing through TTES is 0 for $T_{\mathrm{out,tc}} \le T_{\mathrm{ch,cut\text{-}off}}$ and $\dot{m}_{\mathrm{sto,rated}}$ for $T_{\mathrm{out,tc}} > T_{\mathrm{ch,cut\text{-}off}}$, while in discharging process, the mass flow rate of HTF flowing through TTES is 0 for $T_{\mathrm{out,tc}} \ge T_{\mathrm{dis,cut\text{-}off}}$ and $\dot{m}_{\mathrm{sto,rated}}$ for $T_{\mathrm{out,tc}} < T_{\mathrm{dis,cut\text{-}off}}$.

When HTESS operates in strategy OTC, mass flow rate of HTF flowing through PBTES and TTES is calculated, as depicted in Fig. 5 (b), to make sure the outlet temperature of HTESS is within the allowable temperature range.

2.4. Definition of performance indictor

Utility factor of capacity η_{u} and exergetic efficiency η_{ex} are employed to evaluate the thermal performance of thermal energy storage system. Utility factor of capacity η_{u}, which is defined as the ratio of actually utilized capacity over the nominal capacity, can be expressed as:

$$\eta_{\mathrm{u}} = \frac{Q_{\mathrm{util}}}{Q_{\mathrm{nom}}} \tag{16}$$

where Q_{util} is the actually utilized capacity and can be calculated by Eq. (17); Q_{nom} is the nominal capacity and can be obtained from Eq. (1).

$$Q_{\mathrm{util}} = \int_0^{t_{\mathrm{ch}}} \dot{m}_{\mathrm{HTF}} \rho c_{p,\mathrm{HTF}} (T_{\mathrm{h}} - T_{\mathrm{out}}) \mathrm{d}t \tag{17}$$

The exergetic efficiency η_{ex} in charging-discharging process is defined as:

$$\eta_{\mathrm{ex}} = \frac{Ex_{\mathrm{dis}}}{Ex_{\mathrm{ch}}} \tag{18}$$

where Ex_{dis} and Ex_{ch} are, respectively, the exergy released and stored by thermal energy storage system in the discharging and charging process, which can be calculated by

$$Ex_{\mathrm{dis}} = \int_0^{t_{\mathrm{dis}}} \dot{m}_{\mathrm{HTF}} c_{p,\mathrm{HTF}} \left[T_{\mathrm{out,sys}} - T_{\mathrm{c}} - T_{\mathrm{am}} \ln\left(\frac{T_{\mathrm{out,sys}}}{T_{\mathrm{c}}} \right) \right] \mathrm{d}t \tag{19}$$

$$Ex_{\mathrm{ch}} = \int_0^{t_{\mathrm{dis}}} \dot{m}_{\mathrm{HTF}} c_{p,\mathrm{HTF}} \left[T_{\mathrm{h}} - T_{\mathrm{out,sys}} - T_{\mathrm{am}} \ln\left(\frac{T_{\mathrm{h}}}{T_{\mathrm{out,sys_c}}} \right) \right] \mathrm{d}t \tag{20}$$

where T_{am} is the ambient temperature, which is set to be 25 °C in this study.

2.5. Model validation

The grid independence and time step test are both conducted before simulations. 3 different grid systems of $100(x) \times 10(r)$, $200(x) \times 20(r)$ and $300(x) \times 30(r)$ are tested to calculate the temperature distribution along the packed-bed thermal energy storage at different time, which are shown in Fig. 6 (a). It can be seen that there is little difference between temperature distributions calculated by the grid system of $200(x) \times 20(r)$ and $300\ (x) \times 30(r)$. Thus, the grid system of $300\ (x) \times 30(r)$ is adopted in the following simulations. For the time step test, the simulation results of 3 different time steps (0.2 s, 0.5 s and 1 s) are compared and are illustrate in Fig. 6 (b). It can be seen that 1 s is accurate enough to capture the temperature variation of packed bed thermal energy storage and is used as the time step.

To validate the established model, the results predicted by model employed in this paper are compared with the experimental data by Alam [37] et al. In the experiments, a laboratory scale prototype of packed-bed thermal energy storage filled with encapsulated phase change material is tested between 286 °C and 326 °C. The phase change material is sodium nitrate with melting temperature of 306 °C and the heat transfer fluid is air with volumetric flow rate varying from 110 $m^3\ h^{-1}$ to 151 $m^3\ h^{-1}$. Fig. 7

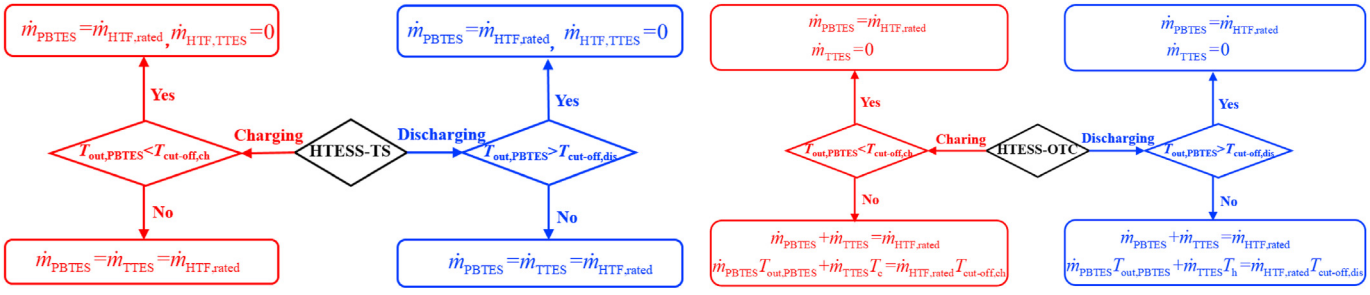

Fig. 5. The calculation process for mass flow rate of HTF through PBTES and TTES in HTESS.

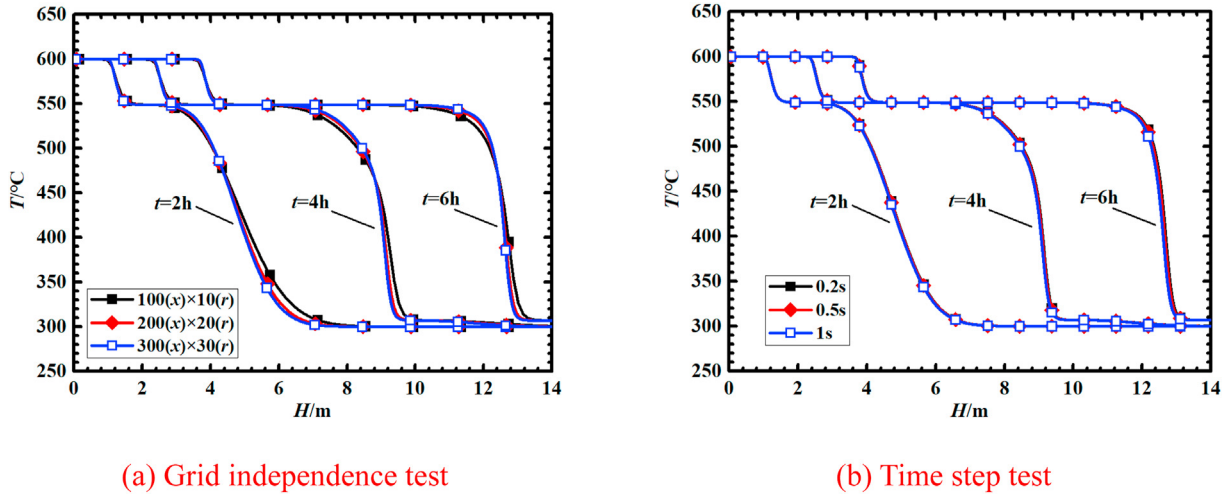

Fig. 6. Grid independence and time step test.

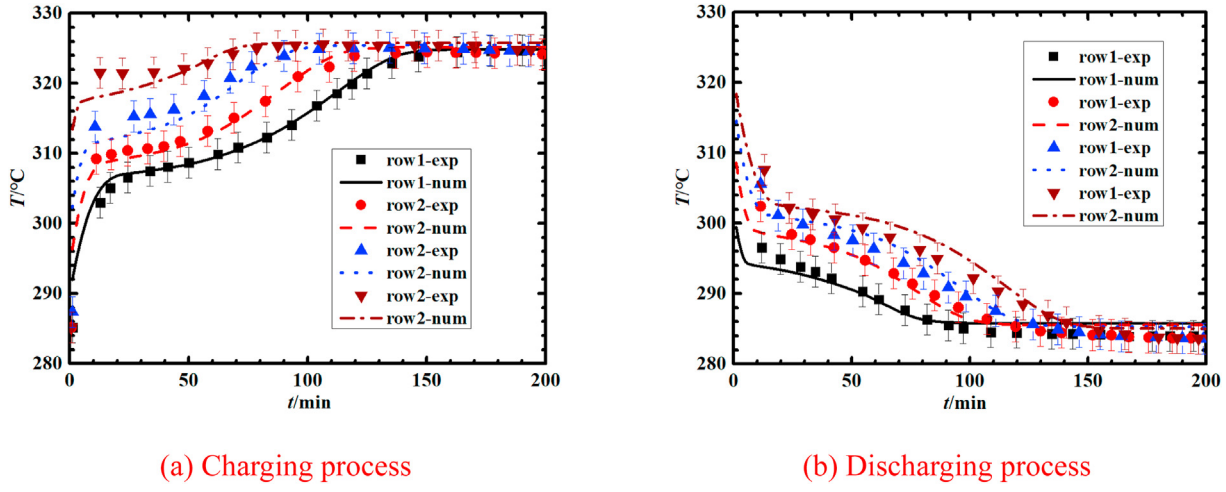

Fig. 7. Comparison of experimental data and numerical results.

presents the comparison of experimental data and numerical results. It can be founded that the temperature distribution of simulation in the axial direction at different charging and discharging time matches well with the experimental measurements, which indicates that the model employed in this study is accurate enough to predict the charging and discharging performance of PBTES with encapsulate phase change material.

2.6. Economic assessment

The total capital cost of thermal energy storage system C_{total} is calculated based on three aspects of cost [25]: heat storage material cost, containment cost and miscellaneous cost [33]. The heat storage material cost contains the cost of heat transfer fluid, phase change material and encapsulation, which are calculated based on the weight of raw material. The containment cost involves the tank cost (stainless steel for hot tank and carbon steel for the cold tank), insulation cost, foundation cost and platform cost, which are calculated based on the surface area. The miscellaneous cost includes the expenditure for distributors, preheating equipment, surge tank, pump, salt melting, piping, valves, instrumentation for electricity and control, which are calculated based on the heat storage capacity of system by interpolating method between typical values of certain capacities. For the economic analysis of the thermal energy storage, the operations and maintenance (O&M) costs are not considered in the economic assessment of thermal energy storage, similar with the work of Ref [18,38–40], because these costs more related with the whole concentrated solar power plant and is calculated based on the electricity produced. Table 4 lists the detailed cost of thermal energy storage system [18].

3. Performance evaluation of stand-alone thermal energy storage system

In this section, for the controlled condition test, thermal and economic performance of different TESS working in stand-alone way after reaching repeatable charging-discharging state are compared. x is the non-dimensional height of PBTES. It should be noted that in PBTES, EPCM with high melting temperature is packed in the upper half of PBTES where x ranges from 0 to 0.5, while EPCM with low melting temperature is packed in the lower half of PBTES where x ranges from 0.5 to 1.

Table 4
Detailed cost of thermal energy storage system [18].

$$C_{TES} = \frac{C_{total}}{Q_{util}} \tag{21}$$

		Unit	Value
Storage material cost	HTF	$\$\cdot ton^{-1}$	1172.6
	HT-PCM	$\$\cdot ton^{-1}$	460
	LT-PCM	$\$\cdot ton^{-1}$	410
	Encapsulation	$\$\cdot ton^{-1}$	750
Containment cost	Stainless steel (321SS)	$\$\cdot m^{-2}$	6332
	Carbon steel	$\$\cdot m^{-2}$	3799
	Insulation	$\$\cdot m^{-2}$	206
	Foundation	$\$\cdot m^{-2}$	1199
	Platform	$\$\cdot m^{-2}$	292
Miscellaneous cost	Distributors	k$	1000
	Preheat equipment	k$	1100-2360 (1000–3000 MWh_{th})
	Surge tank	k$	240-450 (1000–3000 MWh_{th})
	Pump	k$	3890-8670 (1000–3000 MWh_{th})
	Salt melting system	k$	1990-3320 (1000–3000 MWh_{th})
	Piping and valves	k$	1380-2750 (1000–3000 MWh_{th})
	Electrical	k$	298-7320 (1000–3000 MWh_{th})
	Instrumentation and control	k$	293-343 (1000–3000 MWh_{th})

The unit cost for thermal energy storage system C_{TES} can be obtained by Eq. (21).

3.1. Temperature distribution and outlet temperature variation of TESS

Fig. 8 illustrates the temperature distribution of PBTES in different TESS (STESS, HTESS-TS and HTESS-OTC) at the end of charging and discharging process. As can be seen in this figure, at the end of charging process, for STESS and HTESS (HTESS-TS and HTESS-OTC), LTPCM are all melted and HTPCM is partly melted. The melting proportion of HTPCM in STESS which is $x = 0–0.27$ is lowest, then is HTESS-TS with $x = 0–0.37$ and the melting proportion of HTPCM for HTESS-OTC is highest, which is $x = 0–0.40$. Similarly, at the end of discharging process, for STESS and HTESS (HTESS-TS and HTESS-OTC), all the HTPCM are all solidified and only part of HTPCM are solidified. The solidification proportion of LTPCM for STESS which is $x = 0.87–1.0$ is shortest, then is HTESS-TS with $x = 0.84–1.0$, and the solidification range of LTPCM for HTESS-OTC is largest, with $x = 0.80–1.0$. This phenomena indicates that compared with STESS, during the cycle of charging-discharging cycle, the proportion of EPCM in HTESS undergoing the meting-solidification transition is larger, and can store and release more thermal energy, meanwhile the improvement caused by HTESS-OTC is more prominent than HTESS-TS.

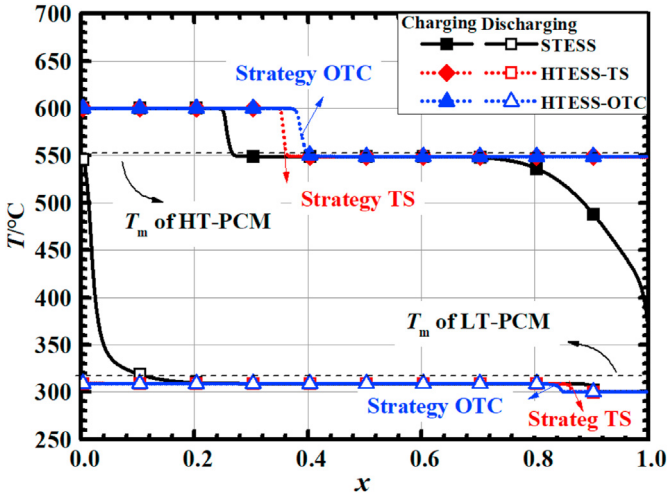

Fig. 8. The temperature distribution of PBTES in different TESS at the end charging and discharging process.

Fig. 9 shows the outlet temperature variation of TESS and PBTES during charging and discharging process. From Fig. 9 (a), it can be seen that outlet temperature of STESS and HTESS (HTESS-TS and HTESS-OTC) all increase initially ($t < 0.8$ h), then keep stable around the melting temperature of LTPCM (308 °C) for a certain duration, and after that the outlet temperature increases again.

(1) For STESS, the charging process ends when the outlet temperature of PBTES (as shown in Fig. 9 (c)) is larger than $T_{ch,cut\text{-}off}$, and the total charging time is 5.65 h.
(2) For HTESS-TS, the thermal energy storage system runs in mode TS-2 after the outlet temperature of PBTES (as shown in Fig. 9 (c)) is higher than $T_{ch,cut\text{-}off}$, and then HTF flowing out of PBTES goes into hot tank to be stored while cold HTF from cold tank flows out of HTESS into solar collection to be reheated again. At this stage, the outlet temperature of thermal energy storage system keeps at 326.4 °C which is stored in the last discharging process and lower than the arithmetic mean value of 510 °C and 300 °C ($T_{dis,\ cut\text{-}off}$). The reason is that in the last discharging process, as shown in Fig. 9 (d), when TTES runs in mode TS-4, the outlet temperature of PBTESS decreases nonlinearly with time. And the decreasing rate of outlet temperature of PBTESS is generally reduced, which lowers the average temperature of molten salt in cold tank. Finally, the total charging time is 6.47 h.
(3) For HTESS-OTC, the thermal energy storage system runs in mode OTC-2 after the outlet temperature of PBTES (as shown in Fig. 9 (c)) is higher than $T_{ch,cut\text{-}off}$. At this stage, the outlet temperature of thermal energy storage system keeps at 390 °Cwhich is equal to $T_{ch,cut\text{-}off}$ until the cold tank is empty, and the total charging time is 7.87 h.

For the discharging process, as can be seen in Fig. 9 (b), the outlet temperature of STESS and HTESS (HTESS-TS and HTESS-OTC) declines initially, and then keeps stable around the melting temperature of HTPCM (550 °C) for a certain duration after which the

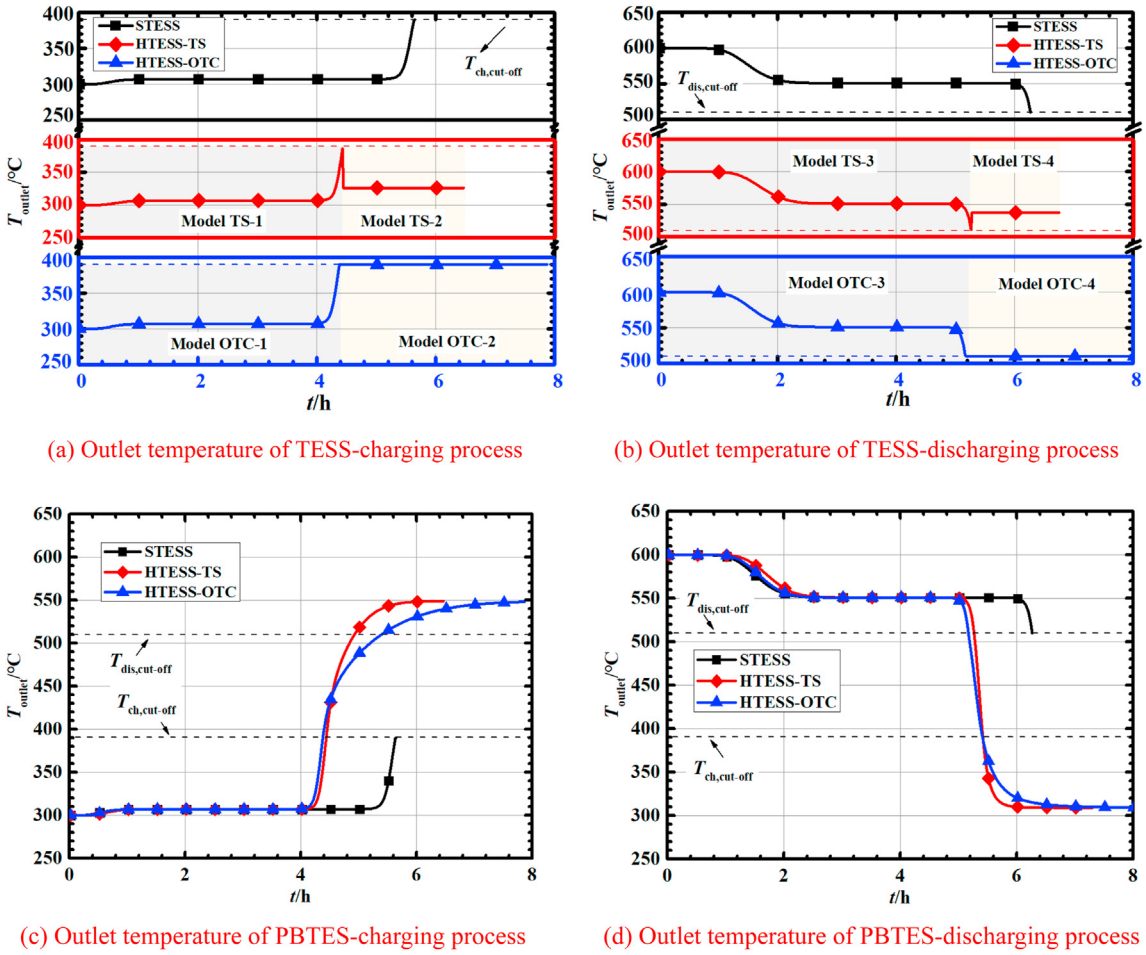

Fig. 9. The outlet temperature variation of STESS and HTESS (HTESS-TS and HTESS-OTC) during charging and discharging process.

outlet temperature decreases again.

(1) For STESS, the discharging process ends when the outlet temperature of thermal energy storage system is lower than $T_{dis,cut-off}$, and the total discharging time is 6.27 h.
(2) For HTESS-TS, the thermal energy storage system runs in mode TS-4 after the outlet temperature of PBTES (as shown in Fig. 9 (d)) is lower than $T_{dis,cut-off}$ ($t = 5.27$ h), and then HTF flowing out of PBTES goes into cold tank for storage while hot HTF from hot tank flows out of thermal energy storage system into power block to generate steam. At this stage, the outlet temperature of thermal energy storage system keeps at 526.4 °Cwhich is stored in the last charging process and higher than the arithmetic mean value of 600 °C and 390 °C ($T_{ch,\ cut-off}$). The reason is that in the last charging process, as shown in Fig. 9 (c), when TTES runs in mode TS-2, the outlet temperature of PBTESS increases nonlinearly with time. And the decreasing rate of outlet temperature of PBTESS is generally reduced, which improves the average temperature of molten salt in hot tank. Finally, the total discharging time is 6.75 h.
(3) For HTESS-OTC, the thermal energy storage system runs in mode OTC-4 after the outlet temperature of PBTES (as shown in Fig. 9 (d)) is lower than $T_{dis,cut-off}$. At this stage, the outlet temperature of thermal energy storage system keeps at 510 °C, which is equal to $T_{dis,cut-off}$, until the hot tank is empty, and the total discharging time is 8.22 h.

From the analysis above, it can be concluded that compared to STESS, the total charging time of HTESS-TS and HTESS-OTC are extended by 14.5% and 39.3% respectively. Meanwhile, the total discharging time of HTESS-TS and HTESS-OTC are extended by 7.7% and 31.1%.

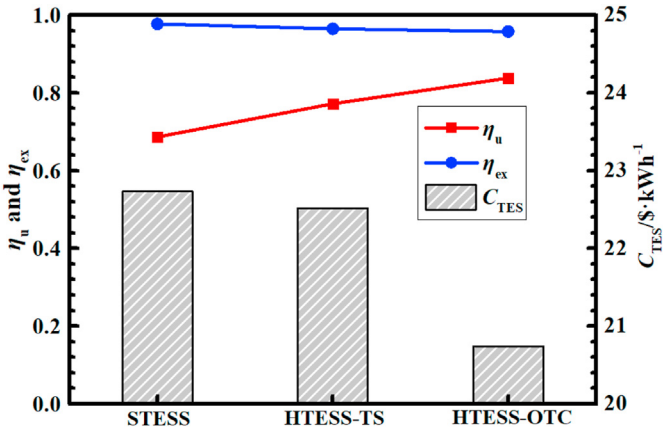

Fig. 10. The thermal and economic performance comparison between different thermal energy storage system after reaching repeatable state.

3.2. Thermal and economic performance comparison between STESS and HTESS (HTESS-TS/HTESS-OTC)

Fig. 10 presents the thermal and economic performance comparison between different STESS and HTESS (HTESS-TS and HTESS-OTC) after reaching repeatable state. From Fig. 10 (a), it can be seen that compared with STESS, the utility factor of the HTESS-TS and HTESS-OTC are improved from 0.686 to 0.772 and to 0.838, which account for the improvement of 12.5% and 22.1% respectively. As for the comparison of exergetic efficiency, the exergetic efficiency of STESS is 0.977, meanwhile the exergetic efficiency of HTESS-TS and HTESS-OTC are 0.965 and 0.958 respectively, which can satisfy the goal of exergetic efficiency of 0.95 for thermal energy storage system expected in SunShot project [41]. The exergy loss in HTESS is mainly caused by the mixing of hot and cold HTF.

In the term of economic performance, the unit cost for heat storage of HTESS-TS and HTESS-OTC is lower than that of STESS due to HTESS's higher utility factor. Compared with STESS, the unit cost for heat storage of HTESS-TS and HTESS-OTC are reduced from 22.73 $\$\cdot kWh_{th}^{-1}$ to 22.51 $\$\cdot kWh_{th}^{-1}$ and 20.74 $\$\cdot kWh_{th}^{-1}$ respectively, which account for deduction of 0.9% and 8.6%.

3.3. Effect of cut-off temperature and capacity of two-tank TES on the thermal and economic performance of HTESS (HTESS-TS and HTESS-OTC)

In the study above, $\Delta\overline{T}_{cut-off}$ and x_{TTES} are set to be 0.3 and 0.25 respectively. To further explore the characteristics of HTESS (HTESS-TS and HTESS-OTC), in this section, effects of $\Delta\overline{T}_{cut-off}$ and x_{TTES} on the thermal and economic performance of thermal energy storage system are discussed.

Fig. 11 illustrates the effect of cut-off temperature difference on thermal and economic performance of HTESS-TS and HTESS-OTC. Because when $\Delta\overline{T}_{cut-off}$ is equal to 0.1, for HTESS-TS, the temperature of HTF in cold tank is 558.2 K, which is higher than $T_{dis,cut-off}$ and doesn't meet the limit of outlet temperature, thus HTESS-TS with $\Delta\overline{T}_{cut-off} = 0.1$ is not included in following discussion. From Fig. 11 (a), it can be seen that with the decreasing of $\Delta\overline{T}_{cut-off}$, less capacity of thermal energy storage system can be utilized, and η_u generally declines. Compared with STESS, the reduction of η_u for HTESS is lesser especially when $\Delta\overline{T}_{cut-off}$ is equal to 0.1 where melting temperature of HTPCM is out of the outlet temperature limit for discharging process. As $\Delta\overline{T}_{cut-off}$ decreases from 0.5 to 0.1, η_u of STESS and HTESS-OTC are reduced by 65.5% and 12.4% respectively. Meanwhile, η_u of HTESS-OTC is 0.777 for $\Delta\overline{T}_{cut-off} = 0.1$, which is improved by 217.1% compared with STESS. Also, it can be seen that lowest value of η_u in HTESS-OTC is even larger than highest η_u of STESS for the $\Delta\overline{T}_{cut-off}$ ranging from 0.1 to 0.5. This phenomena indicates that compared with STESS, HTESS-OTC can maintain a more stable and higher η_u under a wide outlet temperature limits. In term of exergetic efficiency, as $\Delta\overline{T}_{cut-off}$ decreases from 0.5 to 0.1, due to reduced temperature difference between the mixed hot and cold HTF, exergetic efficiencies of STESS and HTESS (HTESS-TS and HTESS-OTC) all generally increase.

As for the unit cost for heat storage, for $\Delta\overline{T}_{cut-off}$ ranging from 0.1 to 0.5, C_{TES} of HTESS-OTC is always lower than that of STESS while for HTESS-TS, the unit cost is almost same with that of STESS. The reduction of C_{TES} caused by HTESS-OTC is more prominent for small $\Delta\overline{T}_{cut-off}$. For example, when $\Delta\overline{T}_{cut-off}$ is equal 0.1, C_{TES} of HTESS-OTC is 22.36 $\$\cdot kWh_{th}^{-1}$, which is reduced by 64.6% compared with STESS.

From the analysis above, it can be concluded that compared to STESS, HTESS-OTC can achieve higher η_u and lower unit cost under a wide outlet temperature limits, and is much less sensitive to the variation of outlet temperature limit which is benefit for the choice of EPCM.

Fig. 12 illustrates the effect of x_{TTES} on the thermal and economic performance of HTESS (HTESS-TS and HTESS-OTC). As is shown in Fig. 12 (a), with the increase of x_{TTES}, η_u of HTESS-TS and HTESS-OTC are both improved gradually due to the raised capacity for thermocline storage or outlet temperature controlling of TTES. When x_{TTES} is improved from 0.25 to 0.75, η_u of HTESS-TS and HTESS-OTC are, respectively, boosted by 19.2% and 17.5%, which are largely higher than that of STESS. As for the exergetic efficiency shown in Fig. 12 (b), as x_{TTES} increases, the exergy efficiency of HTESS-TS increases because of less mixing of hot and cold HTF from thermocline layer. Meanwhile, the exergy efficiency of HTESS-OTC declines generally. This phenomena is caused by the fact that when x_{TTES} is higher, more HTF of two-tank TES is used to mix with HTF from PBTES for the outlet temperature maintaining of HTESS-OTC and larger exergy loss is induced.

As for the economic performance, when x_{TTES} increases, the unit cost of HTESS-TS decreases at first, and reaches the lowest unit cost at $x_{TTES} = 0.5$, then increases again. This can be explained by that when x_{TTES} is relatively large, the improvement of η_u caused by increasing x_{TTES} is small and cannot compensate the increases of the total cost. For HTESS-OTC, the unit cost decreases with the

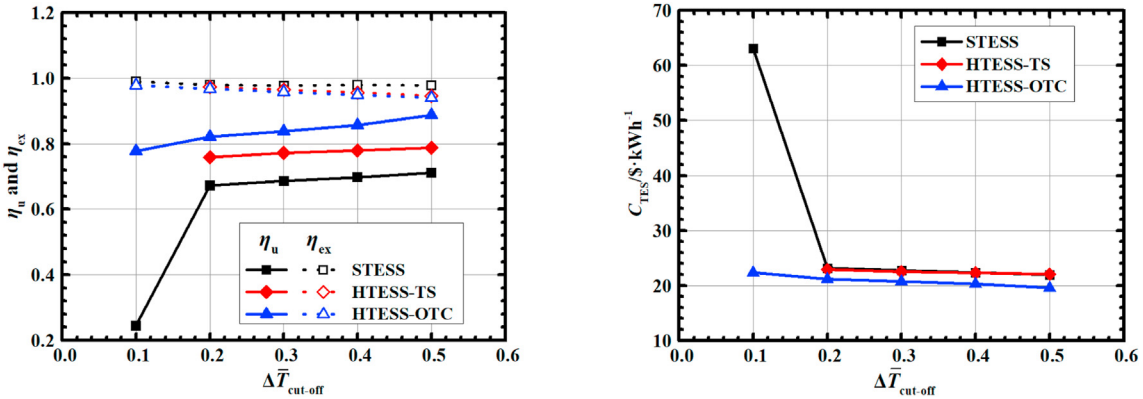

(a) Thermal performance (b) Economic performance

Fig. 11. The effect of cut-off temperature difference on thermal and economic performance.

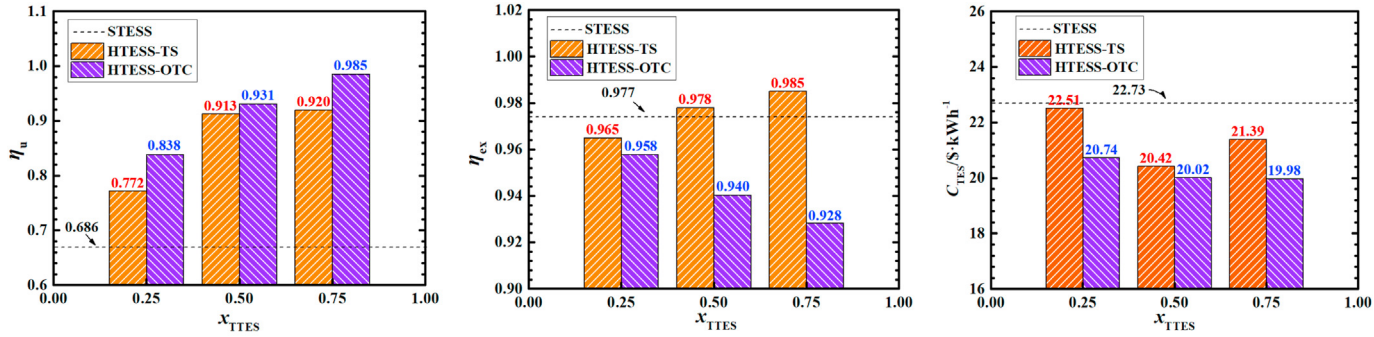

(a) Utility factor of capacity (b) Exergetic efficiency (c) Unit cost for heat storage

Fig. 12. Effect of x_{TTES} on the thermal and economic performance of HTESS (HTESS-TS and HTESS-OTC).

rising of x_{TTES} due to the large improvement of η_u. The lowest unit cost for heat storage of HTESS-TS and HTESS-OTC are 20.42 $\$\cdot kWh_{th}^{-1}$ and 19.98 $\$\cdot kWh_{th}^{-1}$ respectively, which are reduced by 10.2% and 12.1% compared with STESS separately.

4. Performance evaluation of CSP plant integrated with STESS and HTESS (HTESS-TS/HTESS-OTC) under realistic weather condition

To explore the realistic heat storage performance of different thermal energy storage systems, in this section, model of CSP plant integrated with different TESS is established. Then, the running performance of CSP with different TESS in typical day (sunny day and cloudy day) are tested and the annual performance is explored.

4.1. Model establishment of CSP plant integrated with different TESS

Concentrated solar power plant is composed with 3 main components: solar collection system, thermal energy storage system and power block system. In present study, CSP plant model with net output power of 100 MW_e is established [31]. All of the models are established and integrated in software Matlab.

(1) Solar collector

Tower collector is selected to collect solar energy and to heat HTF. The solar multiply (*SM*) is fixed at 2.3 [31], and the rated heat absorbing rate can be calculated by:

$$P_{rec,nom} = SM\frac{P_{PB,rated}}{\eta_{PB,rated}} = 623.1\ MW_{th} \tag{22}$$

The nominal solar radiation intensity I_{nom} is set to be 1000 W m^{-2}. The surround heliostat field is chosen due to its lower levelized electricity cost than north heliostat field for large plants [42]. The annual optical and receiver efficiency of the Central Receiver are set to be 60% and 80% in simulations, which are the average values for large-scale solar thermal power plant with surround heliostat field and are calculated by DELSOL and SAM respectively in Ref. [42]. These typical values have also been used within previous studies of solar power tower plant [27]. Thus, the required mirror area can be obtained by Eq. (23).

$$A_{mirror} = \frac{P_{rec,nom}}{\eta_{rec}\eta_{opt}I_{nom}} \tag{23}$$

HTF flowing from thermal energy storage system and power block are mixed and then flows into solar collector to be heated to T_h. The inlet temperature of solar collector can be obtained by Eq. (24). And the mass flow rate of HTF in solar collector is calculated through Eq. (25).

$$T_{rec,in} = \frac{T_{out,sto}\dot{m}_{sto} + T_{out,PB}\dot{m}_{PB}}{\dot{m}_{sto} + \dot{m}_{PB}} \tag{24}$$

$$\dot{m}_{rec} = \frac{P_{rec}}{c_{p,HTF}(T_{rec,out} - T_{rec,in})} \tag{25}$$

where $T_{out,PB}$ is the outlet temperature of power block, which is designed to be 300 °C. $T_{rec,out}(t)$ denotes the outlet temperature of solar collector and is fixed at 600 °C.

The minimum solar radiation intensity for turbine operating with rated output power is:

$$I_{min} = \frac{P_{PB,rated}}{\eta_{PB,rated}\eta_{rec}\eta_{opt}A_{mirror}} = 434.8\ W\cdot m^{-2} \tag{26}$$

(2) Thermal energy storage

To achieve high utility factor and exergetic efficiency with low unit cost for heat storage at the same time, x_{TTES} is designed to be 0.25 in simulations. The model of thermal energy storage is described in section 4.2.

(3) Power block

Steam Rankine power cycle is adopted to generate power. The parameters of steam Rankine power cycle are obtained from the power model of Flueckiger et al. [31], which can reveal the performance of power block operating at rated and unrated state.

At rated state, the inlet and out temperature of power block are 600 °C and 300 °C respectively. The rated thermal-to-electricity efficiency is 0.4116, and the mass flow rate of HTF flowing through power block can be calculated by

$$\dot{m}_{PB,rated} = \frac{P_{PB,rated}}{\eta_{PB,rated}c_{p,HTF}(T_{in,PB,rated} - T_{out,PB,rated})} \tag{27}$$

At unrated state, the mass flow rate of HTF and output power can be expressed as formulas of HTF's inlet temperature, which are Eq. (28) and Eq. (29) respectively [31].

$$\frac{P_{PB}}{P_{PB,rated}} = -1.706\overline{T}_{in,PB}^{3} + 4.406\overline{T}_{in,PB}^{2} - 2.031\overline{T}_{in,PB} + 0.3307 \tag{28}$$

$$\frac{\dot{m}_{PB}}{\dot{m}_{PB,rated}} = -0.5976\overline{T}_{in,PB}^{3} + 0.399\overline{T}_{in,PB}^{2} + 1.431\overline{T}_{in,PB} - 0.2325 \tag{29}$$

where $\overline{T}$ is the non-dimensional temperature, which is defined as:

$$\overline{T} = \frac{T - T_c}{T_h - T_c} \tag{30}$$

(4) Model integration

Based on the intensity of solar radiation, CSP plant can operate at two different modes.

Mode 1: *DNI* is higher than I_{min}. At this mode, the thermal energy storage system is in charging process, and power block runs at rated state. Mass flow rate of HTF flowing through TESS can be calculated by Eq. (31).

$$\dot{m}_{sto} = \begin{cases} \dot{m}_{rec} - \dot{m}_{PB,rated} & T_{out,sto} \le T_{ch,cut-off} \\ 0 & T_{out,sto} > T_{ch,cut-off} \end{cases} \tag{31}$$

Mode 2: *DNI* is lower than I_{min}. At this mode, the thermal energy storage system is in discharging process. When outlet temperature of TESS $T_{out,sto}$ is equal to T_h, the power block runs at rated state. When $T_{out,sto}$ is in the range of from $T_{dis,cut-off}$ to T_h, the power block runs at unrated state. And when $T_{out,sto}$ is lower than $T_{dis,cut-off}$, the power block and the discharging process of TESS is stopped. The calculation process of mass flow rate $\dot{m}_{sto}$ in TTES is expressed by Eq. (32).

$$\dot{m}_{sto} = \begin{cases} \dot{m}_{PB,rated} - \dot{m}_{rec} & , T_{out,sto} = T_h \\ \text{Iterative calculating} & , T_{dis,cut-off} \le T_{out,sto} < T_h \\ 0 & , T_{out,sto} < T_{dis,cut-off} \end{cases} \tag{32}$$

where the iterative calculating procedure is performed by using Eq. (28) and Eq. (29). Fig. 13 shows the iterative calculating procedure of mass flow rate in TTES。

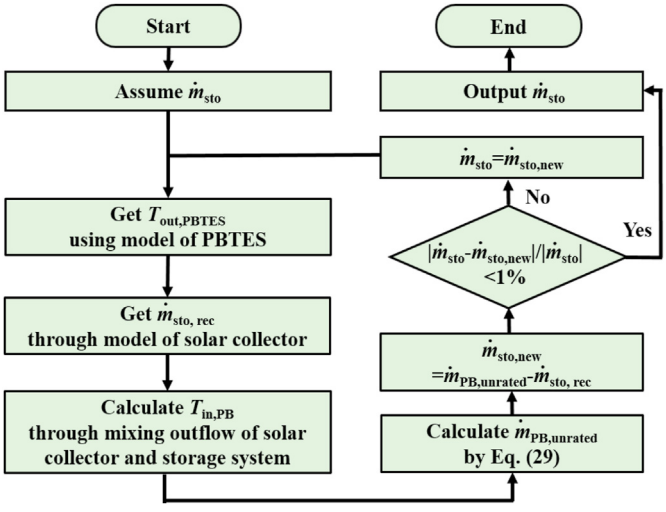

Fig. 13. Iterative calculating procedure of mass flow rate in TTES.

4.2. Evaluation indicator for CSP plant integrated with different TESS

The time averaged utility factor of TESS $\overline{\eta}_u$, solar-to-electricity $\overline{\eta}_{sol-ele}$ and improvement of generated electricity contributed by TESS $\Delta W_{ele,TES}$ are adopted to evaluate the performance of CSP plant integrated with different TESS.

The time averaged utility factor of TESS $\overline{\eta}_u$ can be expressed as Eq. (33).

$$\overline{\eta}_u = \frac{\sum_{i}^{days} \eta_{u,i}}{days} \tag{33}$$

where $\eta_{u,i}$ is the maximum utility factor of TESS in i th day.

The time averaged solar-to-electricity efficiency $\overline{\eta}_{sol-ele}$ is defined as

$$\overline{\eta}_{sol-ele} = \frac{\int_{days} P_{PB} dt}{\int_{days} A_{mirror} I dt} \tag{34}$$

The improvement of generated electricity contributed by TESS $\Delta W_{ele,TES}$ can obtained through Eq. (35).

$$\Delta W_{ele,TES,days} = \int_{days} P_{PB} dt - \int_{days} P_{PB,NS} dt \tag{35}$$

where $P_{PB,NS}$ represent the output power of CSP plant without TESS.

4.3. Daily and annual performance comparison of CSP plant integrated with different TESS

In this section, CSP plant integrated with different TESS are simulated for an entire year, and the daily and annual performance are compared. The solar radiation data is obtained from the NREL's database measured at the location of 39.742° North, 105.18° West during the year of 2018 [43].

At first, two typical weather conditions (sunny day of 2018/06/02 and cloudy day of 2018/06/07, Mountain Standard Time) are selected to compare the daily performance of CSP plant integrated with different TESS. Fig. 14 (a) and (b) illustrate the utility factor and electricity power variation of CSP plant integrated with different TESS under sunny day respectively. As is shown in Fig. 14 (a), as time goes on, *DNI* generally increases. When *DNI* is higher than I_{min}, η_u of different TESS are improved until reaching the maximum value. η_u of STESS reaches its maximum value of 0.689 at 11:50 firstly, then is HTESS-TS with the maximum η_u of 0.765, and HTESS-OTC is the latest to reach its maximum η_u of 0.838. When *DNI* is lower than I_{min} at 19:35, the TESS is switched into discharging process and then η_u decreases generally. In this discharging period, the discharging process of STESS is the shortest, then is HTESS-TS, and total discharging process of HTESS-OTC is longest. As for the electricity power variation, as can be seen in Fig. 14 (b), after *DNI* is lower than I_{min}, CSP plant can sustain the rated power generation for a certain term, and then declines generally. Among these different TESS, the total electricity generation time of STESS (20.4 h) is the shortest, then is HTESS -TS (21.6 h), and HTESS-OTC has the

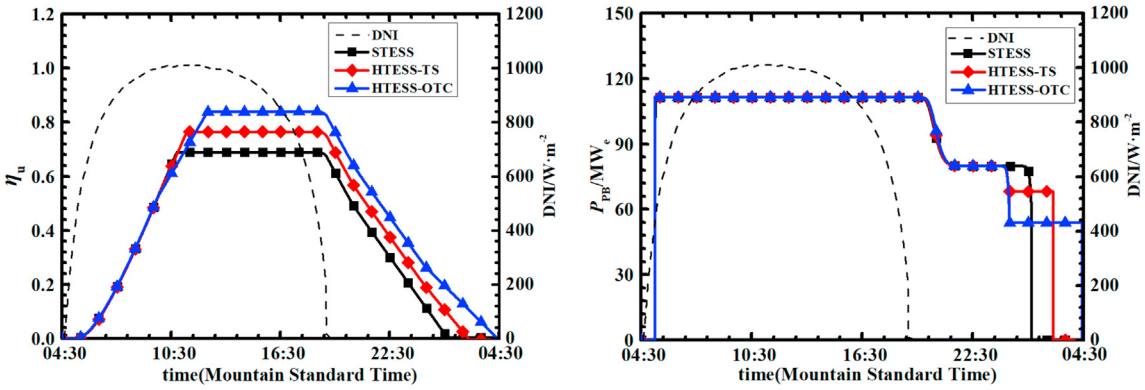

Fig. 14. Utility factor and electricity power variation of CSP plant integrated with different TESS under sunny day.

longest total electricity generation time of 23.15 h which is nearly an entire day.

Fig. 15 (a) and (b), separately, show the utility factor and electricity power variation of CSP plant integrated with different TESS under cloudy day. As can be seen from this figure, in the cloudy day, the utility factor and electricity power variation curve of different TESS almost coincide. The reason of this phenomena is that under the cloudy weather, the solar radiation fluctuates heavily and frequently, thus the TESS switches between charging process and discharging process repeatedly. The highest utility factor during the cloudy day of different TESS are almost same equal to 0.547, which is below their own maximum utility factors, thus the difference of maximum heat storage capacity between different TESS has negligible effect on the utility factor and electricity power variation of CSP plant under cloudy day.

Fig. 16 presents the daily performance of CSP plant integrated with different TESS under different weather condition. As can be seen from Fig. 16 (a), under the sunny weather, compared with STESS, $\Delta W_{ele,TES}$ of HTESS with strategy TS and strategy OTC are boosted by 10.0% and 19.1% respectively, due to their improved maximum utility factor. And the daily solar-electricity efficiency $\overline{\eta}_{sol-ele,sunny}$ are also improved. Meanwhile under the cloudy weather, as shown in Fig. 16 (b), the maximum utility factor and solar-electricity efficiency of CSP with different TESS are almost same. In addition, it can be noted that the daily solar-electricity efficiency of CSP plant under cloudy day $\overline{\eta}_{sol-ele,cloudy}$ is slightly larger than that under sunny day, and this is caused by fact that in sunny day, solar energy is abundant which is beyond the capacity TESS can store and large amount of solar energy is discarded after TESS reaches its maximum utility factor.

Fig. 17 (a) and (b) illustrate the monthly and annual performance of CSP plant integrated with different TESS respectively. As shown in Fig. 17 (a), for each month, the monthly electricity generation of CSP plant is improved with the increase of solar energy. And in general, the solar energy during summer month is larger than that of winter month. As for the annual performance, from Fig. 17 (b), it can be seen that the annual-averaged utility factor of HTESS-TS and HTESS-OTC can reach 0.569 and 0.588 respectively, which are improved by 9.2% and 14.0% compared with that of STESS. And the annual solar-to-electricity efficiency relatively increases by 3.7% for HTESS-TS and 5.6% for HTESS-OTC, compared with STESS. Correspondingly, additional electricity generation induced by TESS has been improved by 9.8% and 14.1% respectively, indicating that HTESS (HTESS-TS and HTESS-OTC) can greatly improve the utility factor and boost the electricity generation for CSP plant.

The analysis is conducted under the assumption that x_{TTES} is equal to 0.25. Then, the influence of x_{TTES} on annual performance of CSP plant integrated with different TESS is analyzed, which is illustrated in Fig. 18. It can be seen that for HTESS-TS, with the increase of x_{TTES}, the annual solar-to-electricity efficiency and additional electricity generation induced by TESS both generally

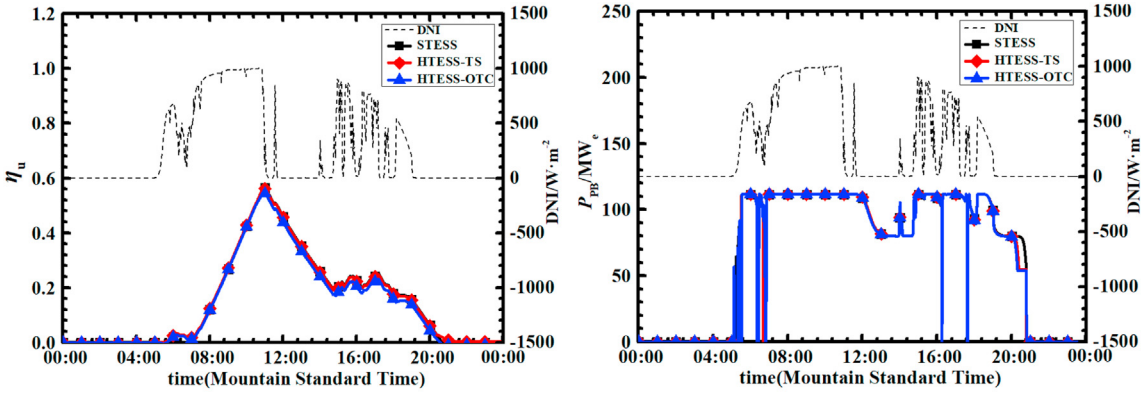

Fig. 15. Utility factor and electricity power variation of CSP plant integrated with different TESS under cloudy day.

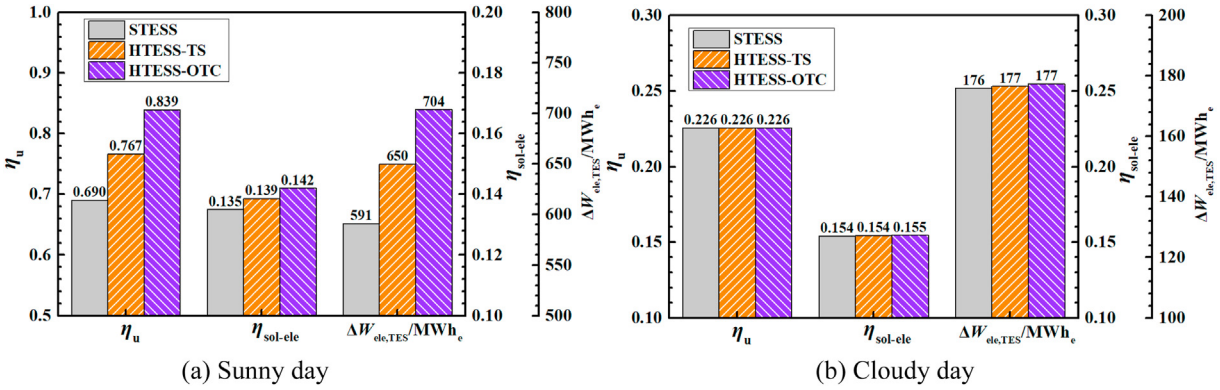

Fig. 16. Daily performance of CSP plant integrated with different TESS under different weather condition.

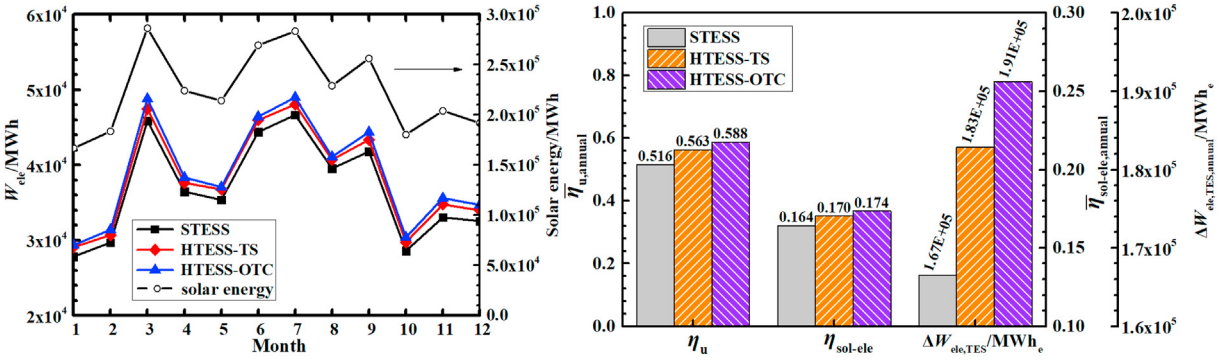

Fig. 17. Annual performance comparison of CSP plant integrated with different TESS.

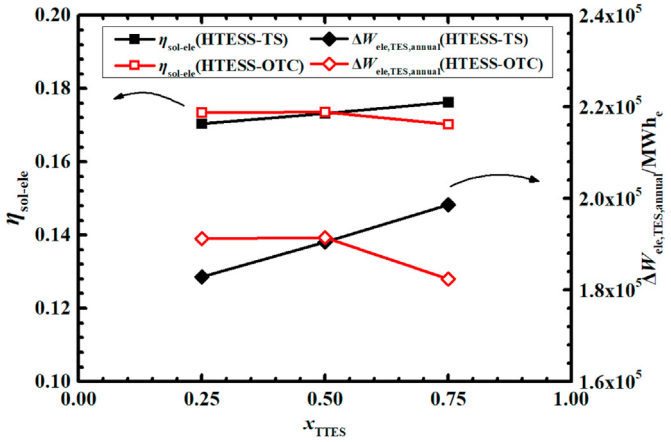

Fig. 18. Influence of x_{TTES} on annual performance of CSP plant integrated with different TESS.

increase. This fact is due to the improved utility factor of capacity and exergetic efficiency with the increase of x_{TTES}, as illustrated in Fig. 12 (a) and (b). However, for HTESS-OTC, as x_{TTES} increases from 0.25 to 0.75, the annual solar-to-electricity efficiency and additional electricity generation induced by TESS both increase at first and then decrease. This phenomena is caused by different changing trends of two key factors: the increasing of utility factor and the decreasing of exergetic efficiency. Thus, for HTESS-TS and HTESS-TS, the additional electricity generation induced by TESS can reach the maximum value of 198,627 MWh and 191,443 MWh at x_{TTES} of 0.75 and 0.5 respectively.

From the analysis above, it can be concluded that to achieve the lowest unit cost for heat storage, HTESS-OTC with $x_{TTES}$of 0.5 is recommended for its low unit cost and relatively high additional electricity generation induced by TESS. On the other hand, to achieve the highest additional electricity generation induced by TESS, the HTESS-TS with $x_{TTES}$of 0.75 is recommended.

5. Conclusion

In this study, new hybrid thermal energy storage system designs and the corresponding operation strategies are proposed to 1) improve the utility factor of PBTES filled with EPCM and 2) reduce the effect of outlet temperature limits for easy application of PBTES filled with EPCM. Firstly, hybrid thermal energy storage system designs and their operation strategies are proposed and presented in detail. Then, the stand-alone thermal and economic performance of single-tank thermal energy storage system and hybrid thermal energy storage are compared with respect to thermal and economic performance. Next, parametric studies of cut-off temperature during charging/discharging process and thermal capacity ratio of two-tank TES in HTESS are conducted to further explore the characteristics of hybrid thermal energy storage systems. Finally, under the realistic solar radiation, the daily and annual performance of concentrated solar power plant integrated with different thermal energy storage systems are compared and discussed. The salient findings are as follows:

(1) Compared with STESS, utility factors of the HTESS-TS and HTESS-OTC are improved by 12.5% and 22.1% with high exergetic efficiency respectively. In term of economic performance, the unit cost for heat storage of HTESS-OTC is 8.6% lower than that of STESS.
(2) Compared to STESS, HTESS-OTC can achieve higher utility factor and lower unit cost for a wide outlet temperature limits, and is much less sensitive to the variation of outlet temperature limit which is beneficial for the choice of EPCM.
(3) In the sunny day, $\Delta W_{ele,TES}$ of HTESS-TS and HTESS-OTC are enhanced by 10.0% and 19.1% respectively compared with STESS due to the improved maximum utility factor. Meanwhile under the cloudy weather, the performance of CSP with different TESS are almost same, because of their same and low highest utility factor during the violent and frequent fluctuation of solar radiation.
(4) Compared with STESS, annual solar-to-electricity efficiencies of HTESS-TS and HTESS-OTC increase by 3.7% and 5.6% respectively. Correspondingly, additional electricity generation induced by HTESS-TS and HTESS-OTC have been improved by 9.8% and 14.1% respectively, indicating that HTESS(HTESS-TS and HTESS-OTC) can greatly enhance the annual electricity generation for CSP plant.

Credit author statement

Zhao Ma: Conceptualization, Methodology, Investigation, Formal analysis, Validation, Writing - original draft. Ming-Jia Li*: Writing - review & editing, Conceptualization, Project administration, Supervision, Funding acquisition. K. Max Zhang: Writing - review & editing. Fan Yuan: Investigation, Validation.

Declaration of competing interest

The authors declare that they have no known competing financial interests or personal relationships that could have appeared to influence the work reported in this paper.

Acknowledgement

This research is supported by the National Natural Science Foundation of China (No. 52076161).

The authors would also like to thank the Foundation for Innovative Research Groups of the National Natural Science Foundation of China (No.51721004) and the Foundation for San Qin Scholar Innovative Research Groups of Shaanxi Province.

References

[1] Li MJ, Tao WQ. Review of methodologies and polices for evaluation of energy efficiency in high energy-consuming industry. Appl Energy 2017;187:203–15.
[2] He YL, Qiu Y, Wang K, Yuan F, Wang WQ, Li MJ, et al. Perspective of concentrating solar power. Energy 2020;198:117373.
[3] He YL, Wang K, Qiu Y, Du BC, Liang Q, Du S. Review of the solar flux distribution in concentrated solar power: non-uniform features, challenges, and solutions. Appl Therm Eng 2018;230:448–74.
[4] Li MJ, Qiu Y, Li MJ. Cyclic thermal performance analysis of a traditional single-layered and of a novel multi-layered packed-bed molten salt thermocline tank. Renew Energy 2018;118:565–78.
[5] Ma Z, Yang WW, Yuan F, Jin B, He YL. Investigation on the thermal performance of a high-temperature latent heat storage system. Appl Therm Eng 2017;122:579–92.
[6] Yuan F, Li MJ, Ma Z, Jin B, Liu ZB. Experimental study on thermal performance of high-temperature molten salt cascaded latent heat thermal energy storage system. Int J Heat Mass Tran 2018;118:997–1011.
[7] Ma Z, Yang WW, Li MJ, He YL. High efficient solar parabolic trough receiver reactors combined with phase change material for thermochemical reactions. Appl Energy 2018;230:769–83.
[8] Liu M, Tay NS, Bell S, Belusko M, Jacob R, Will G, et al. Review on concentrating solar power plants and new developments in high temperature thermal energy storage technologies. Renew Sustain Energy Rev 2016;53:1411–32.
[9] Wang K, He YL. Thermodynamic analysis and optimization of a molten salt solar power tower integrated with a recompression supercritical CO2 Brayton cycle based on integrated modeling. Energy Convers Manag 2017;135:336–50.
[10] Ju X, Xu C, Wei G, Du X, Yang Y. A novel hybrid storage system integrating a packed-bed thermocline tank and a two-tank storage system for concentrating solar power (CSP) plants. Appl Therm Eng 2016;92:24–31.
[11] Pacheco JE, Showalter SK, Kolb WJ. Development of a molten-salt thermocline thermal storage system for parabolic trough plants. J Sol Energy Eng 2002;124(2):153.
[12] Ma Z, Li MJ, Yang WW, He YL. General performance evaluation charts and effectiveness correlations for the design of thermocline heat storage system. Chem Eng Sci 2018;185:105–15.
[13] Wu M, Xu C, He YL. Cyclic behaviors of the molten-salt packed-bed thermal storage system filled with cascaded phase change material capsules. Appl Therm Eng 2016;93:1061–73.
[14] Zhao BC, Cheng MS, Liu C, Dai ZM. Cyclic thermal characterization of a molten-salt packed-bed thermal energy storage for concentrating solar power. Appl Energy 2017;195:761–73.
[15] Xu C, Wang ZF, He YL, Li X, Bai FW. Sensitivity analysis of the numerical study on the thermal performance of a packed-bed molten salt thermocline thermal storage system. Appl Energy 2012;92(2):65–75.
[16] Bindra H, Bueno P, Morris JF. Sliding flow method for exergetically efficient packed bed thermal storage. Appl Therm Eng 2014;64(1–2):201–8.
[17] Li MJ, Jin B, Ma Z, Yuan F. Experimental and numerical study on the performance of a new high-temperature packed-bed thermal energy storage system with macroencapsulation of molten salt phase change material. Appl Energy 2018;221:1–15.
[18] Zhao BC, Cheng MS, Liu C, Dai ZM. Thermal performance and cost analysis of a multi-layered solid-PCM thermocline thermal energy storage for CSP tower plants. Appl Energy 2016;178:784–99.
[19] Zhao BC, Cheng MS, Liu C, Dai ZM. System-level performance optimization of molten-salt packed-bed thermal energy storage for concentrating solar power. Appl Energy 2018;226:225–39.
[20] Li MJ, Jin B, Yan JJ, Ma Z, Li MJ. Numerical and Experimental study on the performance of a new two-layered high-temperature packed-bed thermal energy storage system with changed-diameter macro-encapsulation capsule. Appl Therm Eng 2018;142:830–45.
[21] Xu Y, He YL, Li YQ, Song HJ. Exergy analysis and optimization of charging-discharging processes of latent heat thermal energy storage system with three phase change materials. Sol Energy 2016;123:206–16.
[22] Tao YB, Carey VP. Effects of PCM thermophysical properties on thermal storage performance of a shell-and-tube latent heat storage unit. Appl Energy 2016;179:203–10.
[23] Xu C, Wang ZF, He YL, Li X, Bai FW. Parametric study and standby behavior of a packed-bed molten salt thermocline thermal storage system. Renew Energy 2012;48:1–9.
[24] Zanganeh G, Pedretti A, Haselbacher A, Steinfeld A. Design of packed bed thermal energy storage systems for high-temperature industrial process heat. Appl Energy 2015;137:812–22.
[25] Libby C. Solar thermocline storage systems: preliminary design study. Palo Alto: Electric Power Research Institute; 2010.
[26] Geissbühler L, Mathur A, Mularczyk A, Haselbacher A. An assessment of thermocline-control methods for packed-bed thermal-energy storage in CSP plants, Part 1: method descriptions. Sol Energy 2019;178:341–50.
[27] Geissbühler L, Mathur A, Mularczyk A, Haselbacher A. An assessment of thermocline-control methods for packed-bed thermal-energy storage in CSP plants, Part 2: assessment strategy and results. Sol Energy 2019;178:351–64.
[28] Mathur AK, Kasetty RB. Thermal energy storage system comprising optimal thermocline management. 2013. Google Patents.
[29] Bindra H, Bueno P. Optimum process design of packed bed type thermal storage systems and other applications. 2016. Google Patents.
[30] Howes JS, MacNaghten J, Hunt RG. Layered thermal store with selectively alterable gas flow path. 2017. Google Patents.
[31] Flueckiger SM, Iverson BD, Garimella SV, Pacheco JE. System-level simulation of a solar power tower plant with thermocline thermal energy storage. Appl Energy 2014;113(6):86–96.
[32] Bayón R, Rojas E. Simulation of thermocline storage for solar thermal power plants: from dimensionless results to prototypes and real-size tanks. Int J Heat Mass Tran 2013;60:713–21.
[33] Nithyanandam K, Pitchumani R. Cost and performance analysis of concentrating solar power systems with integrated latent thermal energy storage. Energy 2014;64(1):793–810.
[34] Wu M, Xu C, He YL. Dynamic thermal performance analysis of a molten-salt packed-bed thermal energy storage system using PCM capsules. Appl Energy 2014;121:184–95.
[35] Gonzo EE. Estimating correlations for the effective thermal conductivity of granular materials. Chem Eng J 2002;90(3):299–302.
[36] Odunsi AO, O'Donovan TS, Reay DA. Temperature stabilisation in Fischer-Tropsch reactors using phase change material (PCM). Appl Therm Eng 2016;93:1377–93.
[37] Alam TE, Dhau J, Goswami DY, Rahman MM, Stefankos E. Experimental

investigation of a packed-bed latent heat thermal storage system with encapsulated phase change material. In: ASME international mechanical engineering congress and exposition, montreal, Canada. Nov. vols. 14–20; 2014.
[38] Tehrani SSM, Shoraka Y, Nithyanandam K, Taylor RA. Shell-and-tube or packed bed thermal energy storage systems integrated with a concentrated solar power: a techno-economic comparison of sensible and latent heat systems. Appl Energy 2019;238:887–910.
[39] Mohan G, Venkataraman M, Gomez-Vidal J, Coventry J. Thermo-economic analysis of high-temperature sensible thermal storage with different ternary eutectic alkali and alkaline earth metal chlorides. Sol Energy 2018;176:350–7.
[40] Zauner C, Hengstberger F, Mörzinger B, Hofmann R, Walter H. Experimental characterization and simulation of a hybrid sensible-latent heat storage. Appl Energy 2017;189:506–19.
[41] Mehos M, Turchi C, Vidal J, Wagner M, Ma Z, Ho C, et al. Concentrating solar power Gen3 demonstration roadmap. Golden: National Renewable Energy Lab; 2017.
[42] Avila-Marin AL, Fernandez-Reche J, Tellez FM. Evaluation of the potential of central receiver solar power plants: configuration, optimization and trends. Appl Energy 2013;112:274–88.
[43] National Renewable Energy Laboratory. Measurement and instrumentation data center [DB/OL]. https://midcdmz.nrel.gov/apps/sitehome.pl?site=BMS, 2020-04-01.